Modjeski and Masters Modeling of the Fern Hollow Bridge

Pittsburgh, PA

HWY22MH003

(25 pages)

MEMORANDUM

DATE: 5/19/2023

TO: Mr. Dennis Collins, NTSB

FROM: Modjeski and Masters, Inc.

RE: Analytical Modeling of the Fern Hollow Bridge

This memorandum provides the results of supplemental studies into the Fern Hollow Bridge in Pittsburgh, which collapsed on January 28, 2022. These studies were performed by Modjeski and Masters (M&M) for the National Transportation Safety Board (NTSB) using analytical models originally developed by M&M for the Pennsylvania Department of Transportation (PennDOT) [1]. Frank A. Artmont, PhD, PE, Andrew R. Adams, PE, Phil Ritchie, PhD, PE, and Nohemy Galindez, PhD, PE contributed to the content in this report.

1. Background

As an extension of previous numerical modeling of the bridge performed for PennDOT [1], M&M's scope of work for the NTSB was as follows. The demand on and capacity of the column leg B1R were investigated for the following scenarios:

- Deck wearing surface with a thickness equal to that specified in the design plans, ***absent*** the presence of corrosion (as-designed conditions)
- Deck wearing surface with a thickness equal to ***twice*** that specified in the design plans (mimics load at time of collapse), ***absent*** the presence of corrosion (as-designed conditions)
- Deck wearing surface with a thickness equal to that specified in the design plans, ***including*** the presence of corrosion observed at the time of the collapse (as-inspected conditions)
- Deck wearing surface with a thickness equal to ***twice*** that specified in the design plans (mimics load at time of collapse), ***including*** the presence of corrosion observed at the time of the collapse (as-inspected conditions)

2. Determination of Demands on Column Leg B1R at Time of Collapse

2.1. Global Structural Model

A three-dimensional global structural model of the bridge was previously created in LUSAS Bridge software using information from the design drawings [2] to establish the geometry of the model. The work points of each frame were matched to that shown in the design drawings, including the differing inclinations of the legs and the downward longitudinal slope of the girders from west to east. The floorsystem was modeled as shown in the drawings, however, the cross-slope of the deck was neglected for simplicity, as the cross-slope would not have a significant effect on how the loads were distributed to the frames. As such, the tops of the stringer and girder flanges were provided at the same elevation. Overall views of the model are provided in Figure 1 and Figure 2.

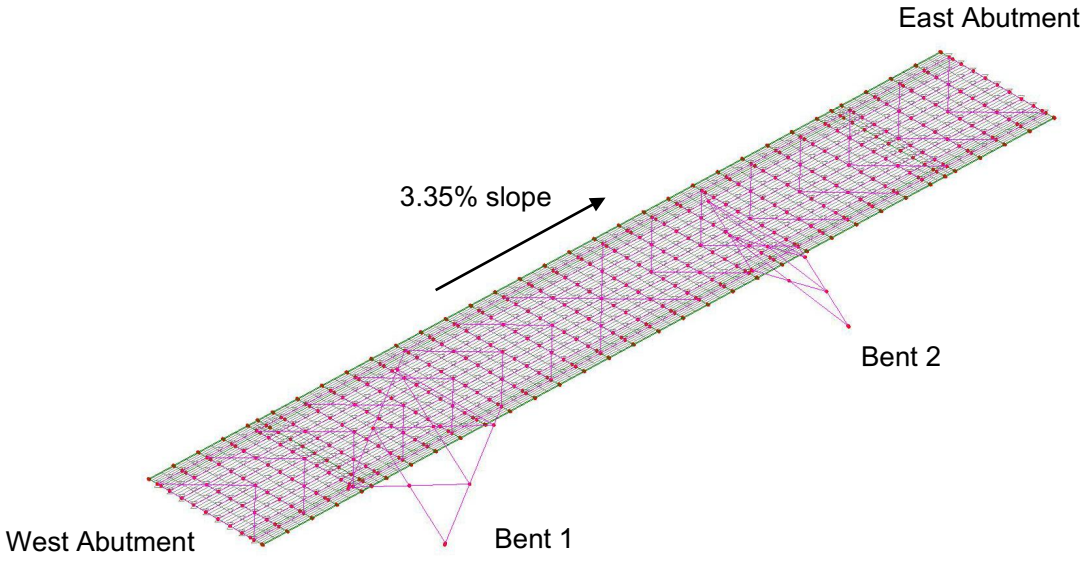

Figure 1 – Global model viewed from above, showing wireframe geometry and mesh.

All axial and flexural members including the girders, inclined column legs, floorbeams, stringers, and bracing were modeled using thick beam elements. The deck was modeled using thick shell elements. In LUSAS terminology, “thick” indicates that shearing deformations are included in the element formulation.

Joint elements were provided between the shell elements of the deck and the beam elements of the girders and stringers, so that adjustable levels of composite behavior could be accommodated. For the global structural models analyzed in this study, these joint elements had large stiffness in the vertical direction, but small stiffness in all other directions, to simulate a non-composite condition of the deck with the girders and stringers as was present in the structure.

Elastic steel material properties (E = 29000 ksi, ν = 0.3) were assumed for all steel components. For the concrete deck, the properties associated with a compressive strength of 4 ksi were

assumed. Note that because of the non-composite behavior, the choice of concrete properties does not significantly affect the structural analysis outcomes.

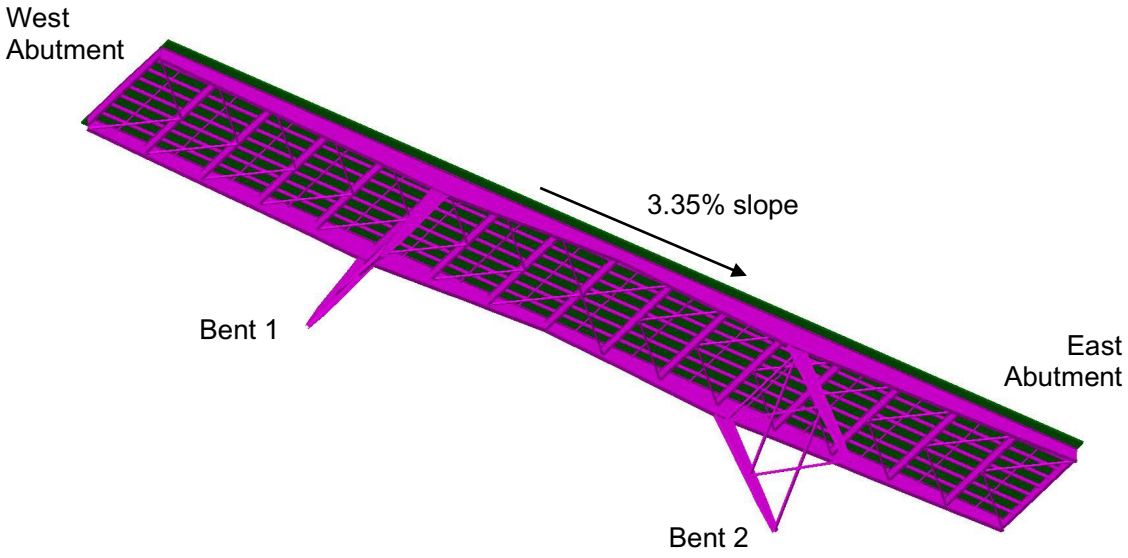

Figure 2 – Global model viewed from below, showing fleshed members.

Vertical displacements at the girder end bearings were restrained; however, all other degrees of freedom were free to translate or rotate. At the bases of the column legs, movements in the vertical, longitudinal, and transverse directions were restrained; however, no rotational restraints were applied.

2.2. Loading

Dead load was calculated implicitly using the cross-sectional areas and densities of the members by applying gravity to these components in the model. This gravity loading was factored up by 6% to account for miscellaneous weights like connection plates, fasteners, reinforcing steel, etc. Distributed line and area loads were added for non-structural components, such as the curb rails, pedestrian railings, and wearing surface. For consideration of cases where the wearing surface load was assumed to be twice that which is shown on the drawings, the distributed area loading representing the wearing surface was doubled.

Live load consisted of the transit bus, which was passed over the structure in the southernmost lane (right lane travelling eastbound). Since only the overall weight of the bus was known at the time the modeling was performed (based on the crane pick weight), the axle loads and weights were assumed based on available information for similar buses and are shown in Figure 3. An empty bus weight is approximately representative of the loading at the time of the collapse given that the bus was carrying only the driver and a few passengers. The bus was moved along the

lane in 1-ft increments, with the responses of the bridge for the bus in each position enveloped together to find the maximum and minimum member forces.

While four other vehicles were also on the bridge at the time of the collapse, due to their relatively light weights in comparison to the bus and the uncertainty as to their position at the time of collapse, it was assumed that these vehicles did not contribute significantly to the axial load in the inclined column legs.

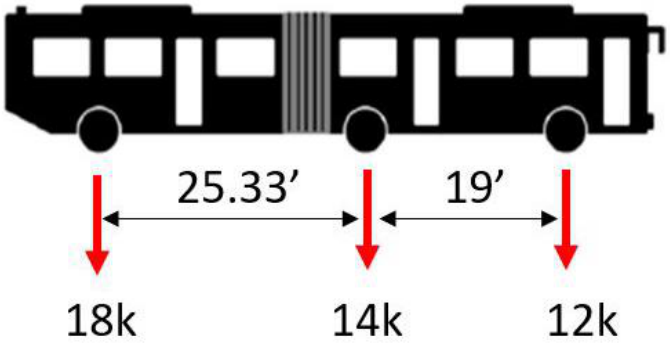

Figure 3 – Assumed axle loads and spacings for transit bus.

2.3. Verification of Model

To verify the model’s behavior, the dead load thrusts and reactions were compared to those listed in the stress sheets of the design drawings. To make this comparison, an additional loading of 250 pounds per linear foot was applied to each girder to be consistent with the assumptions in the stress sheets, as this was listed as additional future loading in the drawings. This load was only used for this comparison and is not included in the demands presented later in this report. The results presented in the remainder of this section include the additional future loading provision.

A comparison of the dead load thrusts and reactions (labeled as shown in Figure 4) between the structural analysis results and stress sheet is shown in Table 1. The values of horizontal and vertical reactions at the bases of the inclined legs compare favorably between the stress sheet and the global structural model.

While the girder end reactions do not compare favorably at first glance (see entries for R_A and R_D), it appears that these reaction values shown in the stress sheet do not include the contribution of the end floorbeam. When this contribution is removed from the LUSAS results such that only the shear force at the girder end is included, the results compare much more favorably (see entries for V_A and V_D).

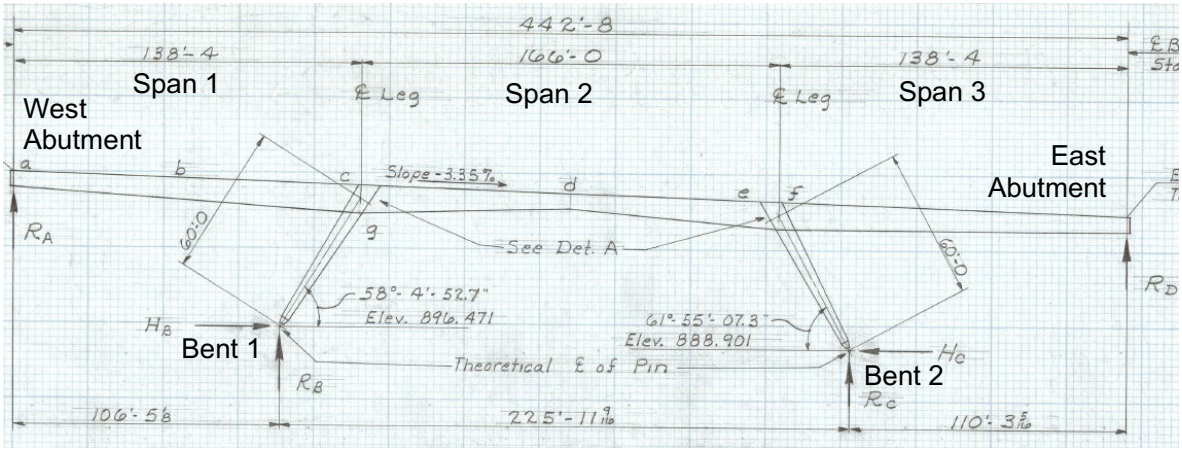

Figure 4 – Diagram of reactions and member force locations from design drawings.

A comparison of dead load axial forces (thrusts) and bending moments is provided in Table 2. The axial forces compare favorably between the stress sheet and global model results, with all values within 5% of each other. The dead load bending moments also generally compare well, although in all cases the global model results show smaller bending moments than the stress sheets. This is due to the flexural stiffness of the floorsystem present in the global model, which would likely have been neglected during the original design of the bridge.

Table 1 – Comparison of Dead Load Reactions between Stress Sheet and Global Model

Location *(refer to **Figure 4**)*	**Dead Load Reactions (kip)**		
	Stress Sheet	**Global Structural Model**	**% Difference**
H_B	589	592	0.5
R_B	1059	1055	-0.3
H_C	589	592	0.5
R_C	1134	1132	-0.2
R_A	234	288	23.1
V_A	234	223	-4.6
R_D	235	288	22.4
V_D	235	222	-5.6

An additional verification of the global model was performed by comparing the camber diagram shown in the drawings with the deflected shape of the global model due to dead load. This comparison is shown graphically in Figure 5 with position of points shown in feet and the deflected

shape/camber amplified 30 times. The largest deviation between the reversed model dead load deflections and the camber shown in the drawings was approximately ¼ inch.

Table 2 – Comparison of Dead Load Axial Forces and Bending Moments between Stress Sheet and Global Model

Location *(refer to **Figure 4**)*	Dead Load Axial Force (kip)			Dead Load Bending Moment (kip-ft)		
	Stress Sheet	Global Model	Difference (%)	Stress Sheet	Global Model	Difference (%)
b	-	-	-	6858	6522	-4.9
d	594	573	-3.5	3770	3202	-15.1
e	619	620	0.2	-17039	-16506	-3.1
f	-	-	-	-17356	-16645	-4.1
g	1177	1173	-0.3	3001	2692	-10.3

Figure 5 – Plot of cambered shape in drawings vs. reversed dead load deflections in analysis mode (longitudinal positions in feet, deformations in feet amplified 30x).

2.4. Global Structural Analysis Results

The axial loading at the base of frame leg B1R (southwest corner) for the as-designed and doubled wearing surface cases are presented in Table 3. Doubling the wearing surface thickness results in the doubling of the wearing surface's contribution to the axial load on the leg. In the as-designed condition, the wearing surface was approximately 14.5% of the total axial load. When doubled however, the wearing surface is approximately 25.3% of the total axial load.

Note that these demands are an estimate based on the best available information regarding the loads present on the leg at the time of the collapse.

Table 3 – Axial Compression Demands at Base of B1R Column Leg

	As-Designed Wearing Surface (kip)	Doubled Wearing Surface (kip)
Unfactored Self-Weight (DC)	988	988
Unfactored Wearing Surface (DW)	174	348
Unfactored Live Load (Transit Bus)	37	37
TOTAL Unfactored Load	1199	1373

3. Determination of Capacity of Column Leg B1R at Time of Collapse

3.1. Introduction to Capacity Calculations

The base of a typical frame leg is shown in Figure 6 [2]. Over most of the frame leg's height, the web depth was tapered, with the flanges inclined at approximately 1.9 degrees from the centerline of the leg. At the base, the flange inclination increased to 22.7 degrees from the centerline of the leg. This local change in inclination of the compression force in the flanges required a tension component to equilibrate the unbalanced force present at this angle change, thus the use of a ¾-inch-thick tie plate spanning between flanges.

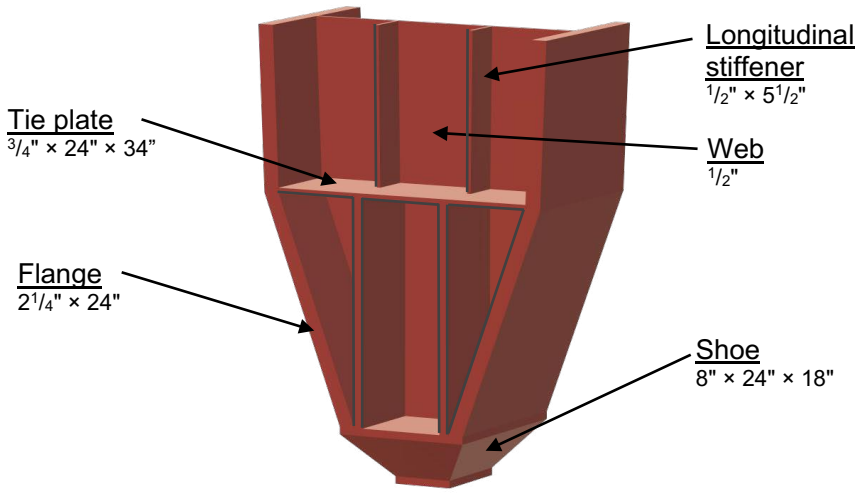

Figure 6 – Base of typical frame leg (looking at inboard side)

Because a failure beginning with the connection between the tie and the downhill (span 2 side) flange is consistent with the post-collapse physical evidence [1,3], the local examination focused

on determining the capacity of this failure mode in terms of axial load applied to the leg and any local secondary load paths that may have been activated based on the initial failure of the tension tie. This was done using the following steps. First, simplified, design-type calculations were performed using the as-designed sizes and strengths of frame leg components to determine the controlling capacity of the leg. Second, local finite element models of the frame leg were developed, using nominal component thicknesses and strengths to develop a refined assessment of the as-designed capacity. Finally, the simplified design-type calculations and local finite element models were revised, including the effects of corrosion and the as-built weld geometry at B1R to estimate the capacity present at the time of collapse.

A summary of the examined cases is provided below, and the methodology behind each will be discussed in the subsequent sections.

- Case A – Hand calculations in the as-designed state[1], assuming global compression failure per the AASHTO LRFD Bridge Design Specifications
- Case B – Hand calculations in the as-designed state, assuming failure of the tie plate in tension causing overall compression failure of the leg
- Case C – Local FEA model in the as-designed state
- Case D – Hand calculations in the as-inspected state[2], assuming global compression failure per the AASHTO LRFD Bridge Design Specifications
- Case E – Hand calculations in the as-inspected state, assuming failure of the tie plate in tension causing overall compression failure of the leg
- Case F – Local FEA model in the as-inspected state, assuming outboard tie-to-flange weld had failed prior to collapse initiation
- Case G – Local FEA model in the as-inspected state, assuming outboard tie-to-flange weld failure during collapse

3.2. Simplified Calculations

The first set of simplified, design-type calculations included calculation of the global compression capacity of the frame leg at its base per the AASHTO LRFD Bridge Design Specifications and using the following assumptions:

- Uniform flange thickness of 2.25 inches
- Uniform web depth of 36 inches
- Effective length factor (K) and unbraced length (L)

[1] "As-designed state" corresponds to models which incorporate the plate thicknesses and weld details as shown on the design drawings.
[2] "As-inspected state" corresponds to models which incorporate the measured plate thicknesses and actual weld details observed in the B1R frame leg.

    - Major Axis: K = 1.0, L = full length of leg
    - Minor Axis: K = 1.0, L = length of leg from base to middle bracing connection
- Local buckling of component plates does not occur (flanges and web meet current AASHTO slenderness requirements, longitudinal stiffeners not included in section property calculations)

Second, the axial compression capacity was calculated as limited by the tension capacity of the tie plate. This was done by calculating the yield capacity of the tie plate and then using statics to calculate the axial force in the leg which would cause this force in the tie plate.

The hand calculations for the global and local compressive strength (as limited by the tie plate capacity) were also computed using the as-inspected thickness of component plates in B1R, which were determined based on the NTSB 3D scan data. The following adjustments were made for these calculations:

- Uniform flange thickness reduced to 2.08 inches
- Uniform web thickness reduced to 0.45 inches
- Uniform tie plate thickness reduced to 0.20 inches
- Due to extreme corrosion at mid-height bracing connections, unbraced length (L) equal to full length of leg for buckling about minor axis

The simplified calculations were focused on the capacity at the base of the leg or in its lower half, and therefore bending moment demands were neglected in these evaluations.

3.3. Localized Finite Element Analysis

Localized finite element analysis (FEA) was conducted using LUSAS Bridge. Local analyses included the entirety of the B1R leg as shown in Figure 7, with a fixed boundary condition at the top to simulate the connection of the leg to the girder. Incremental displacement was applied along the centerline of the leg at the bottom of the shoe to simulate compressive axial load being gradually developed in the leg. The applied displacement increment was adjusted during the nonlinear structural analysis based on convergence. For the bottom half of the leg where local effects were important, e.g., around the tie plate, shell elements were utilized (green in Figure 7). For the upper half of the leg, beam elements were used (pink in Figure 7). Shell elements included shear deformations (thick shell elements in LUSAS terminology) and quadratic shape functions, and the mesh size was 2 inches as shown in Figure 8. Steel material behavior was modeled using the elastic-plastic material properties assuming the von Mises yield criterion.

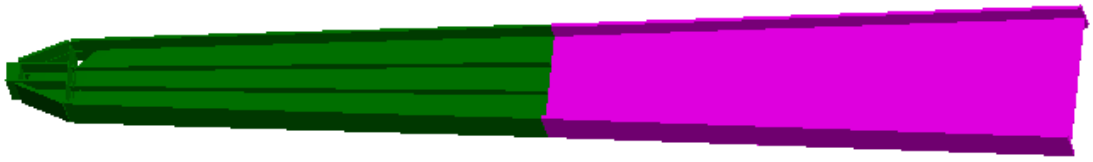

Figure 7 – Local FEA model of frame leg

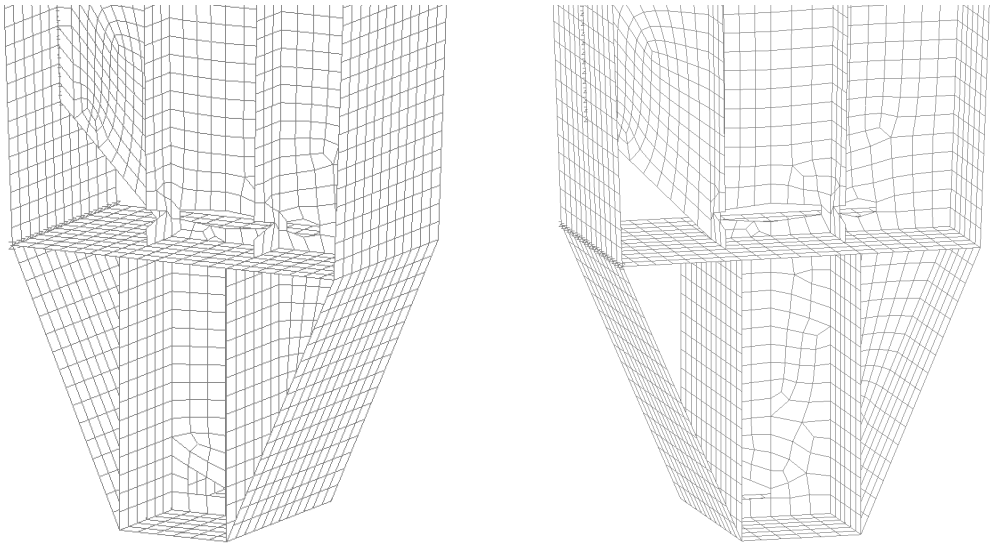

Figure 8 – Views of mesh at base of local FEA model of frame leg for as-inspected model

Two sets of finite element analyses were performed using the local model. The first, shown in Figure 9, was the as-designed condition, where all plates were their nominal sizes without section loss, welds were assumed full penetration per the details on the drawings, and elastic-perfectly plastic material properties using the nominal yield strength of 50 ksi were utilized. The second, shown in Figure 9, was the as-inspected condition, where plates had measured thicknesses as discussed in the next section, welds on the critical failure path (downhill tie plate to flange, downhill flange to shoe, and downhill flange to web) were provided with resistance based on weld fractography studies, holes were introduced in regions of 100% section loss, and the steel material properties included elastic-plastic behavior with strain hardening based on stress-strain behavior determined from testing by the NTSB. As an example, the stress-strain plot with strain hardening used in LUSAS for the as-inspected tie plate is shown in Figure 11.

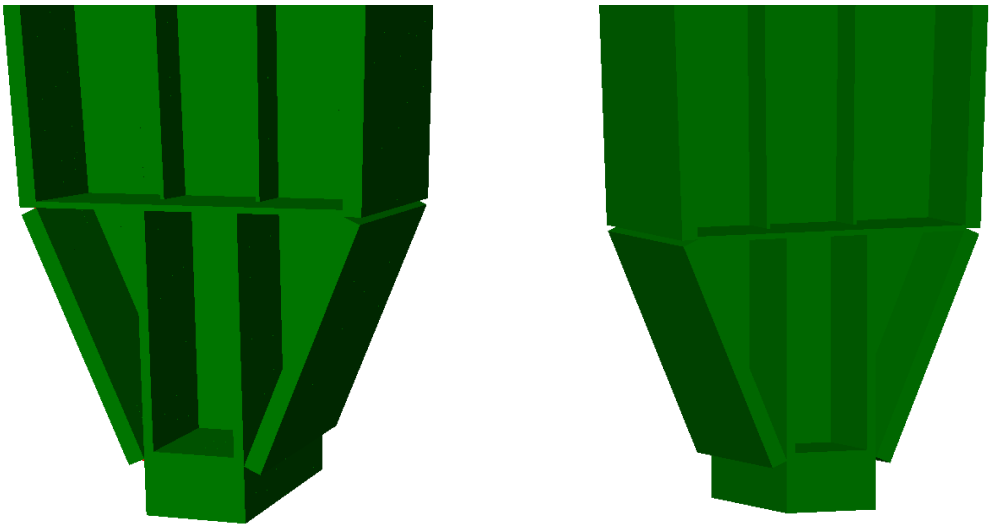

(a) *(b)*

Figure 9 – Fleshed[3] views of base of local FEA model for as-designed condition

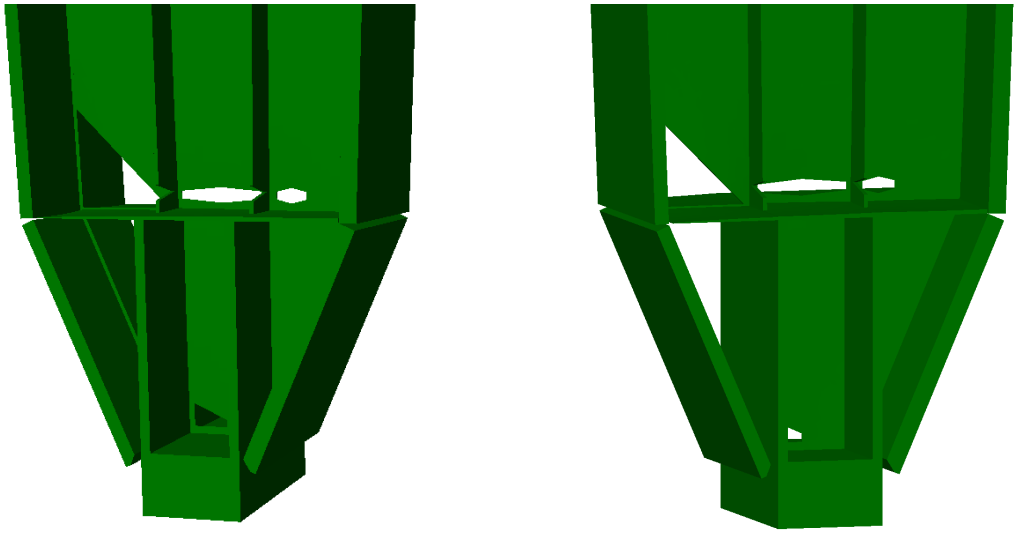

(a) *(b)*

Figure 10 – Fleshed views of base of local FEA model for as-inspected condition

[3] "Fleshed" refers to visualizing the thickness of the shell elements used in the model.

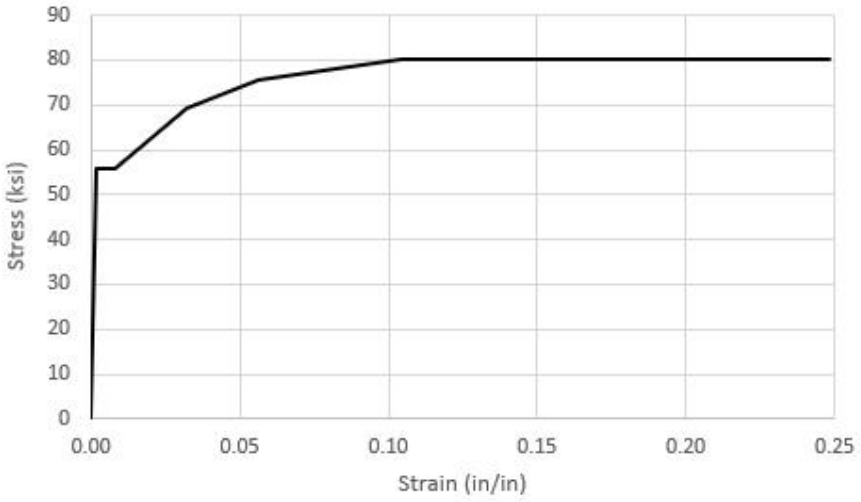

Figure 11 –Stress-strain curve inputted in LUSAS for the B1R tie plate (other component plates were provided similar behavior)

For the as-inspected cases, joint elements were used to simulate fracture of steel components. Joint elements allow for the characterization of the force vs. displacement behavior, allowing for elastic-plastic behavior and subsequent reduction in load due to fracture. Based on field studies and information provided by the NTSB through mechanical test data [4], 3D scan data [5], and weld fractography reports [6], the joint element behaviors assumed for the local modeling were as described below.

For the inboard downhill (span 2) side of the tie plate, the failure appeared to have occurred through the thinnest remaining section of the tie plate (approximately 0.05 in.), as the weld was still intact. As such, the joint elements at this location were assumed to have elastic-plastic behavior up until the moment of fracture, thereafter the force in the joint element reduces to near zero with increasing displacement. While the force-displacement behavior beyond the peak load is not indicative of actual behavior, where all force would be removed instantaneously upon fracture, a more gradual reduction from peak force and minimum load above zero is required for convergence of the nonlinear structural analysis. The force-displacement behavior is based on the stress-strain test data for the tie plate acting over a length of 1 inch with a thickness of 0.05 inches and assuming a 30% reduction in ductility due to the corrosion present (refer to [7]). The force-displacement behavior for the inboard downhill (span 2) side of the tie plate is shown in Figure 12.

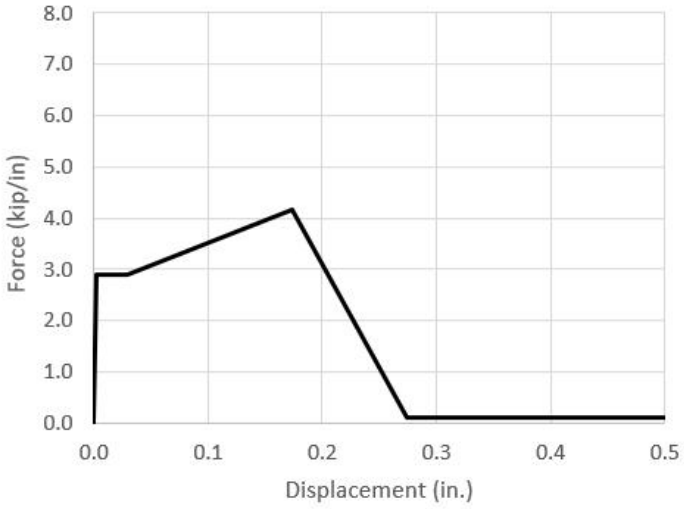

Figure 12 – Joint element behavior for inboard downhill (span 2) side of tie plate (ductile failure through thinnest remaining section).

For the outboard downhill (span 2) side of the tie plate, the failure appeared to have occurred through the welded connection. Based on the NTSB's investigation of the fracture surfaces [6], the welded connection was not full penetration as indicated by the design drawings but was rather a fillet-welded connection or a partial penetration connection with extremely limited penetration into the tie plate and flanges. In addition, the NTSB information revealed that only the weld on the underside of the tie plate was effective, with the weld on the upper side showing signs of limited fusion. Therefore, the joint elements were given similar elastic-plastic-fracture behavior to the inboard side of the tie plate, but the ultimate strength was based on the AASHTO LRFD BDS equations for an assumed weld metal strength of 70 ksi and a minimum throat thickness of the underside fillet weld (approximately 0.36 inches). Yield force was determined as a fraction of this ultimate strength based on tests conducted by Gomez et al. on fillet-welded connections of similar size [8]. Yield and ultimate displacements were also assumed based on tests conducted in the same study [8]. The force-displacement behavior for the outboard downhill side of the tie plate is shown in Figure 13.

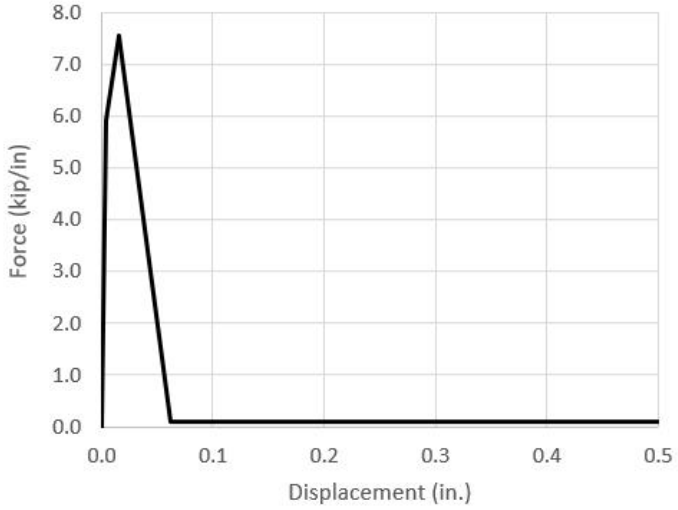

Figure 13 – Joint element behavior for outboard downhill (span 2) side of tie plate (brittle failure through tie plate-to-flange weld).

Near the web-to-flange weld on the downhill side of the B1R leg, it appeared that failure occurred through the thinnest remaining section of web plate (approximately 0.25 inches) adjacent to the weld, as the weld was still intact. As such, the joint elements at this location assumed a similar behavior to the inboard downhill side of the tie plate. The force-displacement behavior was based on the stress-strain test data for the web plate acting over a length of 1 inch with a thickness of 0.25 inches and assuming a 30% reduction in ductility due to the corrosion present (refer to [7]). The force-displacement behavior for the web-to-flange joint elements is shown in Figure 14. These web joint elements were included in the model all the way to the boundary between the shell element portion of the model and the beam element upper portion.

All local FEA cases included geometric nonlinearity though consideration of the co-rotational formulation for beam elements and total Lagrangian formulation for the shell elements. Arc-length control using the Crisfield method was used to ensure convergence in the presence of snap-through/snap-back behavior.

Similar to the simplified calculations, the local FEA cases focused on the capacity at the base of the leg and therefore bending moment demands were neglected in these evaluations.

3.4. Determination of As-Inspected Component Thicknesses

Severe section loss was noted at the base of all four frame legs. As part of their investigation, the NTSB performed 3D laser scanning of the bases of all four frame legs to obtain detailed section loss measurements over all plates comprising the frame leg bases. The results of these laser scans [5] were used as follows to determine thicknesses of plates to use within the as-inspected cases.

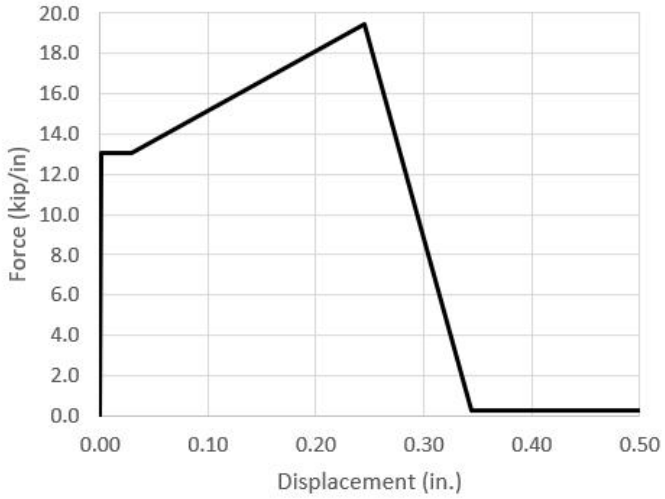

Figure 14 – Joint element behavior for web-to-flange region (ductile failure through thinnest section of web adjacent to flange).

Each component was split into panels according to how they were divided by other components, as shown in Figure 15 for tie plate panels A through F and Figure 16 for web plate panels A through F. For each of these panels, a three-by-three grid of thickness measurements was taken, resulting in nine total data points. An example of this process is shown in Figure 17. These data points were used to fit a mathematical function which could then be input as a thickness variation within LUSAS. The general form of the function was as follows:

$$t = c_1 + c_2x + c_3x^2 + c_4y + c_5xy + c_6x^2y + c_7y^2 + c_8xy^2 + c_9x^2y^2$$

In essence, this function allowed the thickness to vary parabolically in both principal directions. When the function was entered into LUSAS, the as-designed thickness was used as a maximum, and 0.01 inches was used as a minimum thickness, ensuring that the plate would be no thicker than the as-designed condition without corrosion. For regions of 100% section loss, holes were provided directly in the LUSAS model as shown in Figure 9(b).

For the web panel directly below the downhill side of the tie plate (labeled “A” in Figure 16(a)), section loss was assumed as 100%, which is consistent with the degree of corrosion noted post-collapse. For the web panels immediately above the tie plate, the section loss of B1L was assumed as a stand-in for the B1R since the B1R web panels in this location were damaged beyond recognition during the collapse. Based on inspection report pictures, it appears that the B1L leg in this region had a similar corrosion pattern and extent to B1R.

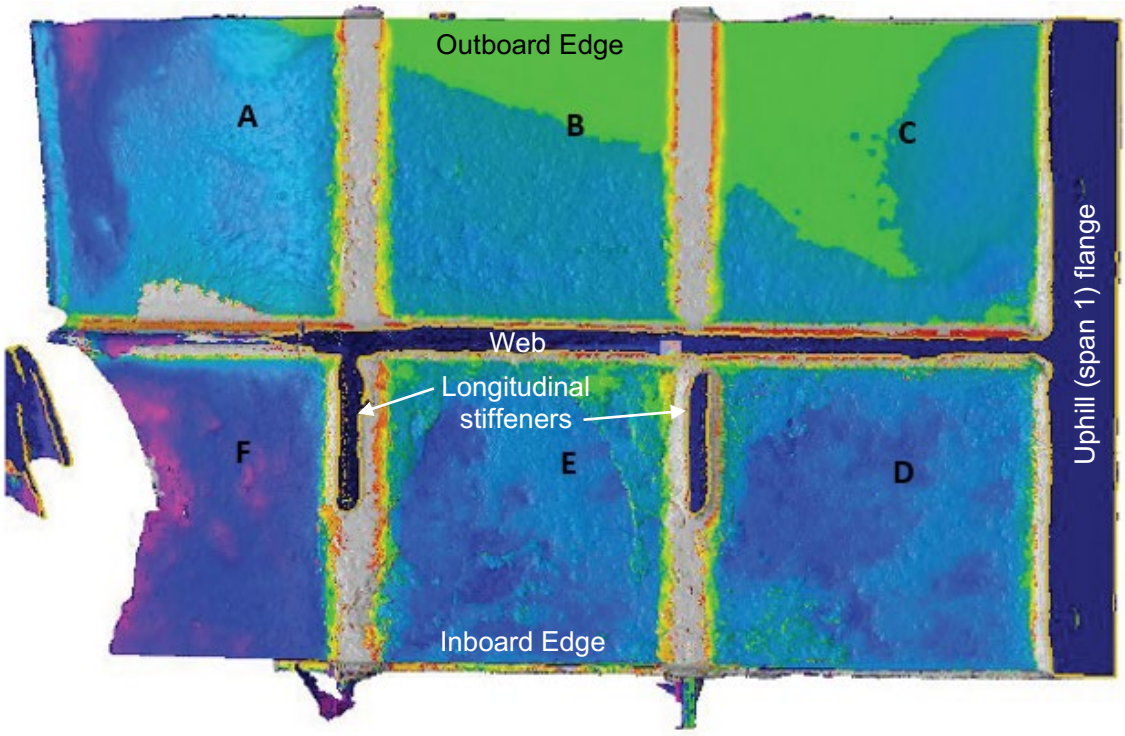

Figure 15 – Plan view of B1R tie plate showing thickness measurements and tie plate panel labels A through F (base images taken from [5] with annotation added)

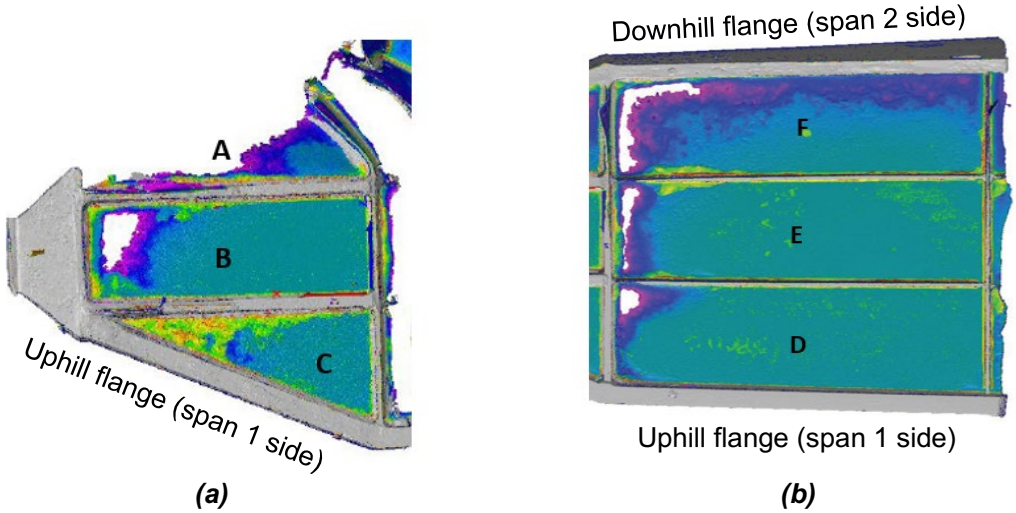

Figure 16 – Elevation view of web looking towards outside of bridge, showing thickness measurements and web plate panel labels A through F for (a) B1R below tie plate and (b) B1L above tie plate (base images taken from [5] with annotation added)

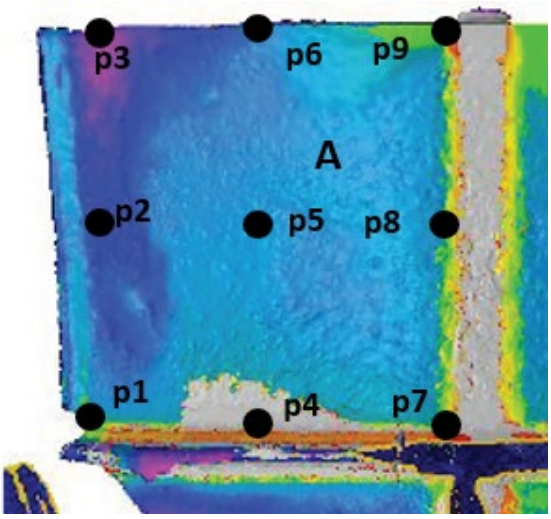

Figure 17 – Measurement points for determining thickness variation in tie plate panel A (refer to Figure 15 for location of tie plate panel A)

3.5. Results

The results of the various capacity calculations are shown in Table 4. In general, all the as-designed cases show a compressive capacity much larger than all the as-inspected results. This is expected due to the significant corrosion present in the frame legs at the time of collapse.

Cases A, B, D, and E are a result of simple hand calculations and therefore a plot of axial load versus displacement along the longitudinal axis of the leg cannot be provided for these analyses. However, the use of the local FEA models for cases C, F, and G allow for the plotting of this type of curve, as shown in Figure 18. Note that case C has a much larger capacity than either of the as-inspected cases and undergoes more displacement prior to ultimate failure. The case C response generally shows linear behavior up until peak load and then the load falls with increasing displacement. The stress state at peak load is shown in Figure 19. Localized yielding in the tie above the lower longitudinal stiffeners leads to the tension load shifting to the web.

The as-inspected cases are plotted on their own in Figure 20 to show more detail. Each of these responses shows “snap-back” behavior with multiple load peaks, where an initial peak load occurs followed by one or more subsequent peak loads. Each of these peaks correspond to different failure modes, which occur sequentially due to the different stiffnesses required to activate each of the modes and the change in load path as the leg redistributes loads. For example, the initial peak load for case F occurs when the inboard side of the tie plate fails, and the secondary peak occurs when the axial load carried by bending in the downhill flanges reaches its maximum load capacity. The stress states at these peak loads are shown in Figure 21. Note that the plasticity of the tie occurs in the joint elements at the flange-to-tie weld, which is why the stresses appear low in the tie in Figure 21.

Table 4 – Summary of B1R Capacities

Case	Condition	Method	Failure Mode	Initial Peak (kip)	Final Peak (kip)
A	As-Designed	By hand	Global Yielding/Buckling	5319	N/A
B	As-Designed	By hand	Tie Yielding	5139	N/A
C	As-Designed	FEA	Tie Yielding	6041	N/A
D	As-Inspected	By hand	Global Yielding/Buckling	2319	N/A
E	As-Inspected	By hand	Tie Yielding	1291	N/A
F	As-Inspected	FEA	Multiple	852	1077
G	As-Inspected	FEA	Multiple	1055	1083

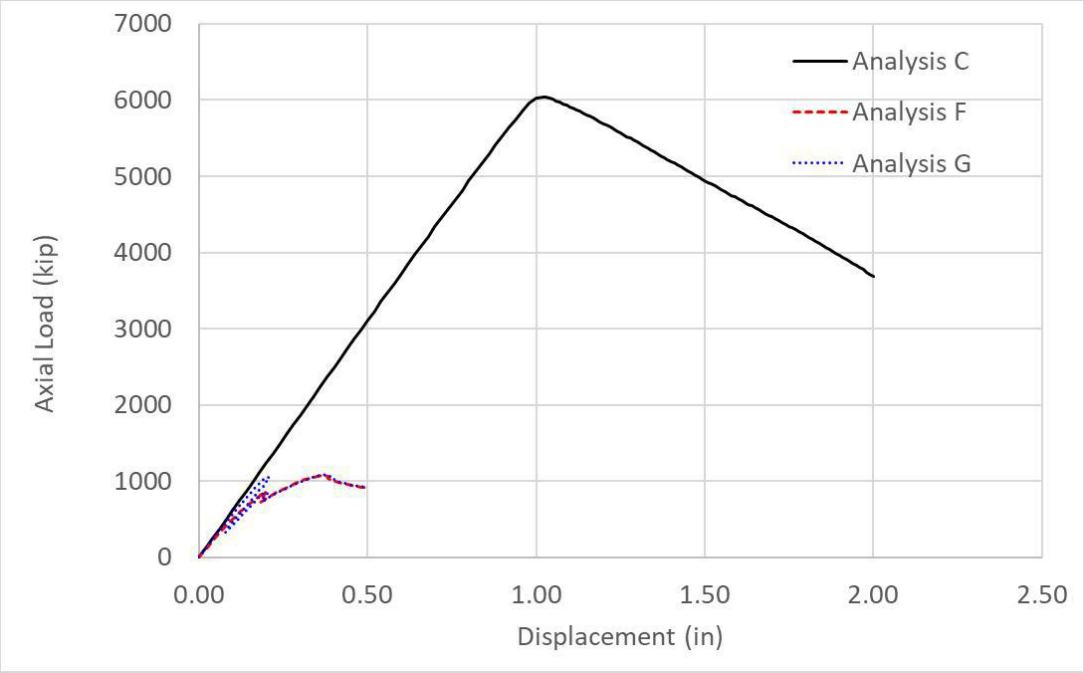

Figure 18 –Axial compression vs. displacement along longitudinal axis of frame leg for all local FEA analyses

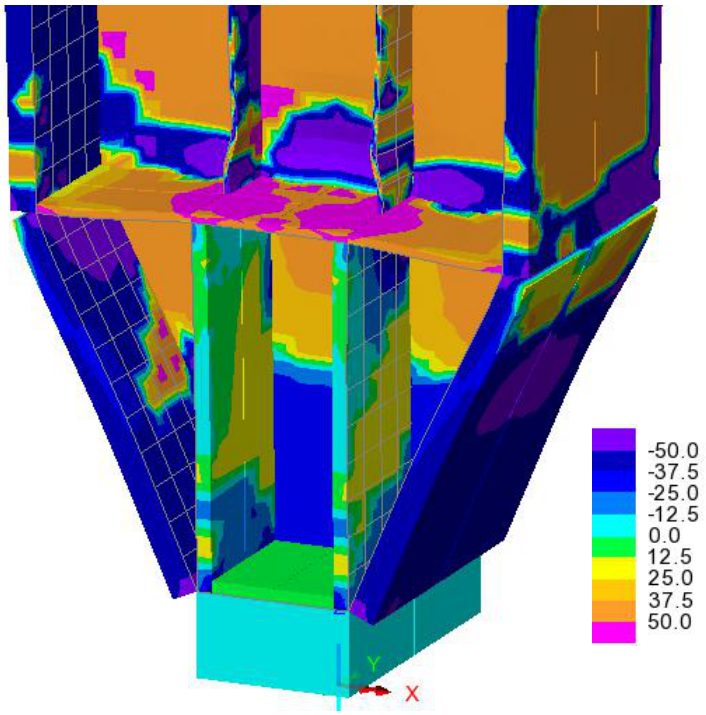

Figure 19 – Signed largest value of principal stress (in ksi) at peak load for case C

Case G is similar in response to case F but contains an additional peak which occurs prior to the initial peak seen in the case F response. This peak is caused by the loading and failure of the weld at the outboard side of the flange. This is the weld that is assumed to have already failed in case F. The secondary peak occurs due to subsequent failure of the inboard side of the flange, and the tertiary peak occurs when axial load carried by bending in the downhill flanges reaches its maximum load capacity. The stress states at the initial peak and tertiary peak load are presented in Figure 22. These stress states are similar to those of case F.

Note that the failures of both cases F and G appear similar to the failure patterns witnessed in the collapsed structure. The failure of the tie along its downhill connection to the flange (where corrosion was largest) side leads to flexure of the flanges. This flexure of the flanges cannot be sustained by the welded connection to the web above the tie nor the welded connection of the flange to the shoe, causing the flange to ultimately separate from both components.

The local finite element analyses are performed by formulating static equilibrium and do not account for inertial effects that accrue when a drop in the load deflection curve occurs and additional deformation is necessary to achieve the subsequent peak load. Given the mass of the bridge, once an initial peak is reached and downward acceleration begins, the presence of secondary and later peaks may not arrest the movement resulting in the capacity being defined by the initial peak.

Given the above, it appears likely that case G is the best approximation of the actual capacity of the bridge at the time of collapse among the different cases investigated herein.

It should also be noted that the results of cases F and G show lower capacity than the simplified hand calculation result of case E. This is due to case E assuming a uniform section loss through the tie plate (intact thickness of approximately 0.20 inches) and yield failure at the thinnest section, like one would assume for design. However, due to the differing failure modes of the tie on the inboard and outboard sides and their differing stiffnesses, the strength of the entire tie cannot be engaged at once, causing a lower overall capacity prior to the flanges being engaged in flexure.

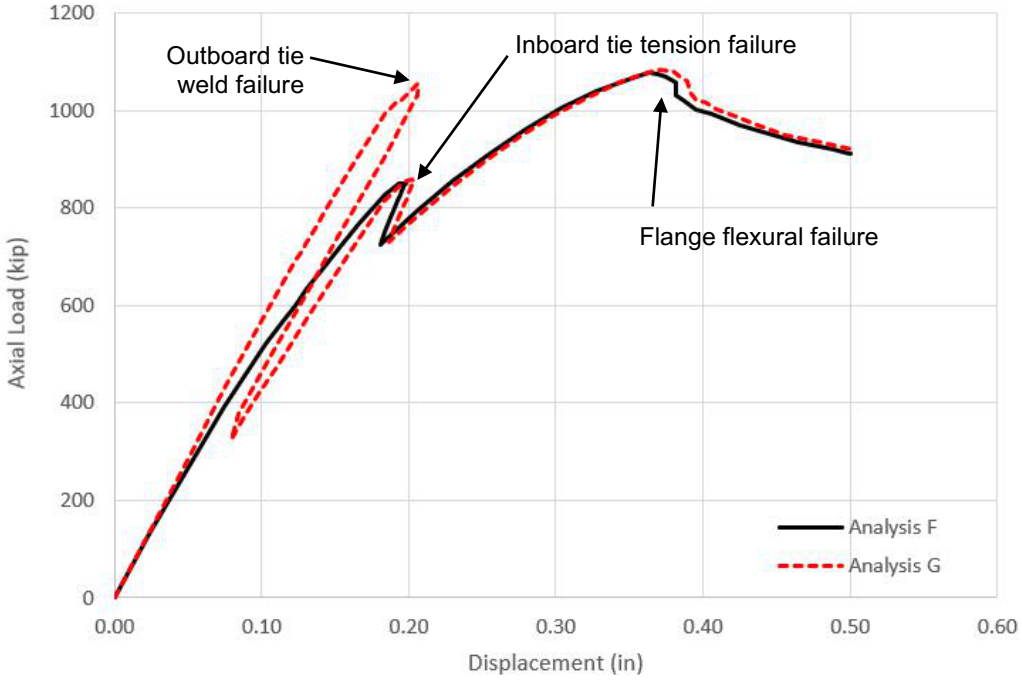

Figure 20 – Axial compression vs. displacement along longitudinal axis of frame leg for as-inspected local FEA analyses

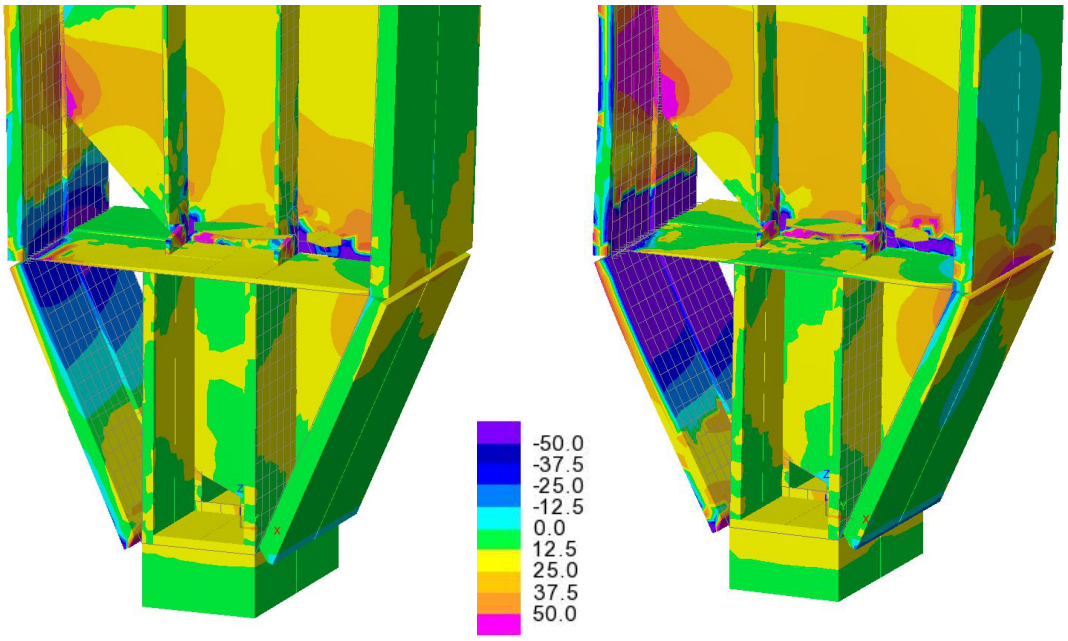

(a) *(b)*

Figure 21 – Signed largest value of principal stress (in ksi) at (a) initial peak load and (b) secondary peak load, for case F

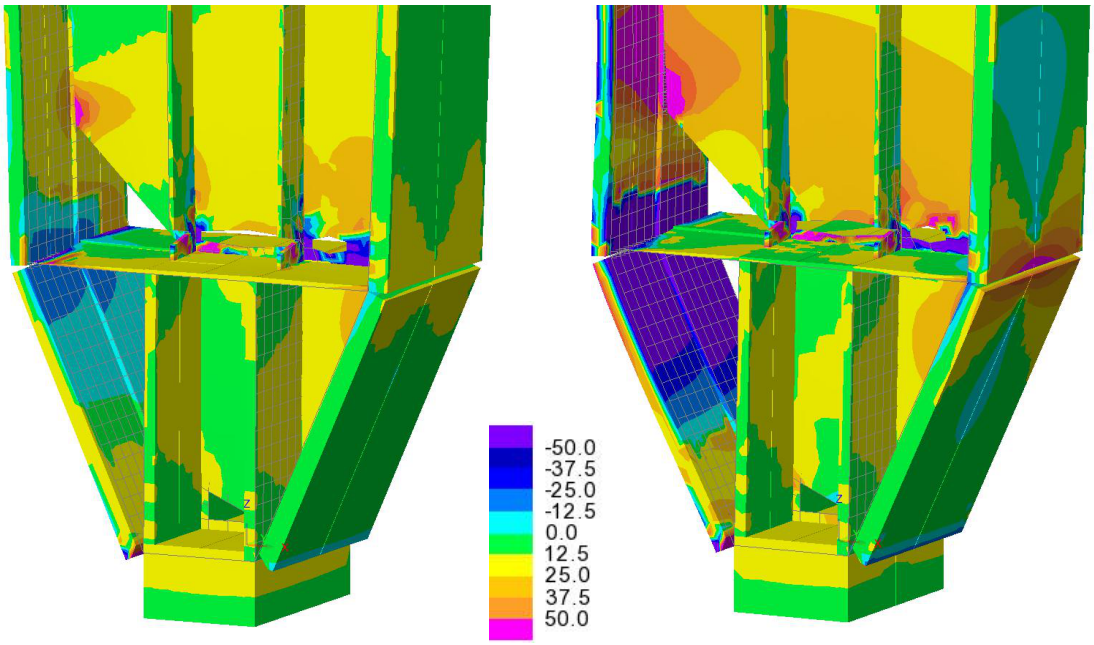

(a) *(b)*

Figure 22 – Signed largest value of principal stress (in ksi) at (a) initial peak load and (b) tertiary peak load, for case G

4. Summary of Demand to Capacity Ratios for Considered Scenarios

The demand-to-capacity (D/C) ratios for unfactored load and resistance are presented in Table 5 and in Figure 23 for all considered cases. For all as-designed cases, the D/C ratios are less than unity, indicating that the design of the leg for axial failure at its base (neglecting the presence of bending moments) was satisfactory to carry the loads estimated to be present at the time of collapse, even for the case of double the as-designed wearing surface thickness being present.

When significant section loss had occurred throughout the leg and in the cross-bracing between legs, a global-type failure was still not expected as indicated by the case D results. However, the D/C ratios of cases E through G indicate that a localized failure in the tie would have been expected based on the doubled wearing surface loading. For the as-designed wearing surface loading, tie failure would be expected for cases F and G.

Table 5 – Summary of Demand-to-Capacity Ratios

Case	Condition/ Method	Capacity (kip)	As-Designed Wearing Surface		Doubled Wearing Surface	
			Demand (kip)	D/C	Demand (kip)	D/C
A	As-Designed By-Hand	5319	1199	0.23	1373	0.26
B	As-Designed By-hand	5139	1199	0.23	1373	0.27
C	As-Designed FEA	6041	1199	0.20	1373	0.23
D	As-Inspected By-hand	2319	1199	0.52	1373	0.59
E	As-Inspected By-hand	1291	1199	0.93	1373	*1.06*
F	As-Inspected FEA	852	1199	*1.41*	1373	*1.61*
G	As-Inspected FEA	1055	1199	*1.14*	1373	*1.30*

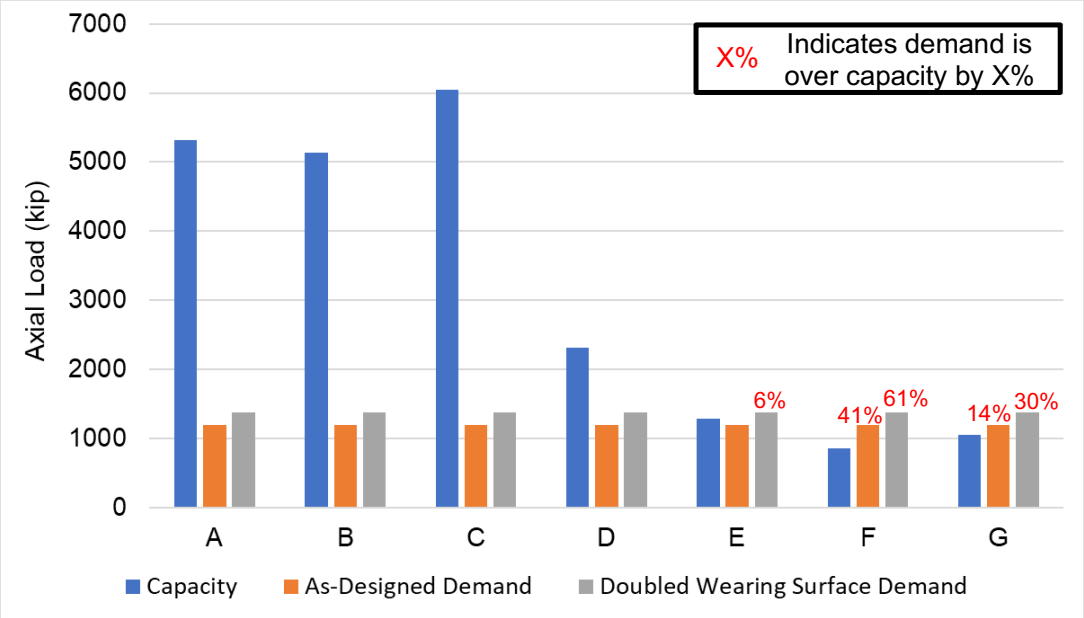

Figure 23 – Graphical summary of demands and capacities for Analyses A through G

5. Summary

Using a global structural analysis model of the bridge, the load in the frame leg B1R was estimated at the time of the collapse. The effect of an increase in the wearing surface thickness on the demands in the leg, over that assumed in the original design, was investigated. Capacities for the leg were estimated using both manual calculation methods as well as refined local finite element models considering the material behavior determined from post-collapse tests, the element thicknesses including section loss due to corrosion determined from 3D scans of the components post-collapse, and the likely weld strengths connecting key components based on sections taken through the welds of the components post-collapse. Consideration of the deformation capacity of the various load paths in the leg is needed to determine an accurate capacity, as not all load paths can develop their peak capacities at the same time.

Thomas P. Murphy, PhD, PE, SE
Senior Vice President / Chief Technical Officer

6. References

[1] Analysis of the Fern Hollow Bridge Collapse – Final Report. Prepared by M&M for PennDOT. In progress.

[2] Reconstruction of Forbes Avenue Bridge over Fern Hollow and Approaches – Design Drawings. Prepared by Richardson, Gordon, and Associates Consulting Engineers. November 1970.

[3] Forbes Avenue Bridge Collapse Forensic Investigation – Draft Preliminary Site Visit Report. Prepared by M&M for PennDOT. January 31, 2022.

[4] Forbes Avenue Over Fern Hollow Bridge Collapse Investigation: Steel Mechanical and Materials Testing Factual Report. Federal Highway Administration. March 1, 2023

[5] NTSB Materials Laboratory Factual Report 23-009 for HWY22MH003

[6] NTSB Materials Laboratory Factual Report 23-034 for HWY22MH003

[7] Ductile Design of Steel Structures – Second Edition. Bruneau, Uang, and Sabelli. 2011.

[8] Strength and Ductility of Welded Joints Subjected to Out-of-Plane Bending. Gomez and Kwan. Published by AISC. 2008.